

Single-Process Fused Filament Fabrication 3D-Printed High-Sensitivity Dynamic Piezoelectric Sensor

Tilen Košir^a, Janko Slavič^{a,*}

^a*University of Ljubljana, Faculty of Mechanical Engineering, Aškerčeva 6, 1000 Ljubljana, Slovenia*

Cite as:

Tilen Košir and Janko Slavič, Single-Process Fused Filament Fabrication 3D-Printed High-Sensitivity Dynamic Piezoelectric Sensor, Additive Manufacturing, 102482, November 2021, <https://doi.org/10.1016/j.addma.2021.102482>

Abstract

Piezoelectric sensors require electric poling to provide piezoelectric properties. Furthermore, for a functional sensor, electrodes need to be deposited on the sensing element, which makes manufacturing the sensor a multi-process. Multi-processing limits the sensor's shape complexity and makes it harder to embed the piezoelectric sensing elements in various 3D-printed structures. Integrating electric poling into the fused-filament-fabrication (FFF) 3D-printing technique was already researched; however, the methods require an additional electrode-deposition process and the piezoelectric sensitivities of the fabricated films were not comparable to conventional methods. This research presents the design principles of a functional, single-process, dynamic piezoelectric sensor using the FFF technique, which includes electrode deposition and electrode poling. A PVDF filament is used to fabricate

*Corresponding author

Email address: janko.slavic@fs.uni-lj.si (Janko Slavič)

the active piezoelectric layer. An Electrifi conductive filament is used to fabricate the electrodes of the piezoelectric film and the wire-like traces connecting the electrodes to the high-voltage terminals. As a result, the sensor undergoes electrode poling in the process of 3D printing. In order to study the piezoelectric response in different directions, two different dynamic sensor designs are presented. The sensor's response to in-plane and out-of-plane loading is measured in terms of the sensor's sensitivity. In-plane and out-of-plane sensitivities were measured for the two presented sensor designs. The proposed design principles for the FFF of piezoelectric sensors enable the single-process manufacturing of geometrically complex sensors and offer the possibility to embed the piezoelectric sensing elements into various FFF structures without an additional process.

Keywords: single process, piezoelectric sensor, piezoelectric effect, poling, fused-filament fabrication, additive manufacturing

1. Introduction

In recent years, additive manufacturing (AM) has been widely used for the manufacturing of sensing elements [1][2]. In 2017, Bodkhe et al. produced a fully functional, 3D-printed, piezoelectric contact sensor [3] using solvent-evaporation-assisted 3D printing (SEA-3DP). In 2017, Thuau et al. developed entirely inkjet-printed, piezoelectric, flexible electronic devices [4]. In 2019, Zega et al. manufactured a three-axis, capacitive-based accelerometer [5] by combining stereolithography (SLA) and wet metallization. In 2019, Emon et al. 3D-printed a stretchable, soft pressure sensor consisting of an ionic-liquid-based pressure-sensitive layer electrically contacted with carbon

nanotube-based stretchable electrodes [6]. In 2020, Xu et al. presented a method for manufacturing a smart, elastomer, cellular foam in a single process, where selected fiber segments can act as a strain sensor in the cellular structure [7]. In 2020, Liu et al. produced a fully printed accelerometer based on piezoresistive principles, using SLA, direct-ink writing [8] and screen-printing techniques.

The fused filament fabrication (FFF), 3D-printing technique is especially promising for manufacturing capacitive, piezoresistive and piezoelectric sensing elements. One of the first successful attempts at the FFF of piezoelectric polyvinylidene fluoride (PVDF) films for sensor applications was presented by Lee and Tarbutton in 2014 [9]. In 2019, Marandi and Tarbutton 3D printed double-layer piezoelectric sensing elements [10]. In 2020, Hohimer et al. developed capacitive-based touch sensors [11]. In 2021 Arh et al. produced a single-axis, fully 3D-printed, piezoresistive accelerometer [12] and Palmieri et al. produced FFF 3D-printed self-aware structures by utilizing 3D-printed piezoresistive sensory element [13].

In the field of FFF piezoelectric sensing, research mostly focuses on the manufacturing of thin piezoelectric films and methods to enhance their piezoelectric sensitivity. Homopolymer PVDF and its copolymer alternative PVDF-TrFe are the most extensively used, commercially available materials, in FFF piezoelectric film fabrication that can be purchased in filament form. The piezoelectric performance of thin PVDF films depends on the amount of semi-crystalline β -phase present in the film [14]. The β -phase is one of the four possible phases PVDF can be morphed into, and has the molecular conformation with the highest net dipole [15]. To achieve high sensitivity, the

molecular dipoles have to be aligned under a high electric-field at a temperature slightly below the Curie temperature [16]. Aligned dipoles are locked as the electric-field is removed, resulting in a piezoelectric film with the desired polarization [17].

Conventional methods of obtaining thin, FFF, 3D-printed piezoelectric sensors usually involve the following three steps: film manufacture, electrode placement and electric poling. The latter two steps can be interchanged, depending on the technique used. Electric poling is used to achieve the desired polarization direction and a better piezoelectric sensitivity. Conventionally, poling is performed using contact-electrode poling [18] or corona poling [19]. To collect the generated charge from the piezoelectric layer, the electrodes need to be applied to the thin piezoelectric film. Several conventional methods for electrode deposition exist, for example, coating [20], screen-printing [21][22], and deposition [23][24]. For applications see [14][25], where the sensing elements showed good sensitivity, although multiple processing steps were involved.

In order to integrate the poling step within the FFF sensor-fabrication step, several methods such as the Integrated 3D-Printing and Corona poling process (IPC) [15] and electric poling-assisted additive manufacturing (EPAM) [26] were developed. In the IPC process presented by Kim et al. [15], the film is fused-filament fabricated in the first step. In the second step, a high voltage is applied to the extruder nozzle. While maintaining a high voltage and temperature, the nozzle follows the previous fabrication path while maintaining a constant gap between the film and the nozzle tip. On the other hand, in the EPAM process presented by Lee et al. [26], the high voltage is

already applied to the nozzle while the PVDF film is being extruded. Both techniques successfully integrate the poling into the FFF process; however, at the cost of a lower film sensitivity compared to the conventional poling techniques used in [14][25]. Furthermore, both techniques require the deposition of electrodes in a separate manufacturing process in order to obtain functional piezoelectric sensing element.

This manuscript proposes a method that fabricates the piezoelectric film and the electrodes, and poles the piezoelectric film in a single process using the FFF, 3D-printing technique and electrode poling. Based on the proposed method, a showcase piezoelectric dynamic sensor was manufactured and its performance was measured in terms of its sensitivity, along with the piezoelectric coefficients. The manuscript is organized as follows: Sec. 2 describes the theoretical background, Sec. 3 describes the design principles of the dynamic sensor design, Sec. 4 describes the experimental methods used in sensor fabrication, poling and sensitivity measurements, Sec. 5 presents the results of the methods used, Sec. 6 is an in-depth discussion of the results and Sec. 7 draws the conclusions.

2. Theoretical Background

Throughout this research, the piezoelectric response directions are defined according to the PVDF print pattern during FFF, as seen in Fig. 1. Using the summation convention and the Voigt notation, the constitutive piezoelectric equations, expressing a linear piezoelectric effect, can be written as [17]:

$$\varepsilon_i = S_{ij}^E \sigma_j + d_{mi} E_m \quad i, j = 1, 2, 3, 4, 5, 6 \quad m = 1, 2, 3 \quad (1)$$

$$D_m = d_{mi} \sigma_i + \xi_{mk}^\sigma E_k \quad i = 1, 2, 3, 4, 5, 6 \quad m, k = 1, 2, 3 \quad (2)$$

where ε_i is the strain component, E_m is the electric field component, S_{ij}^E is the compliance coefficient at a constant electric field, σ_i is the stress component, d_{mi} is the piezoelectric coefficient, D_i is the electric displacement and ξ_{ik}^σ is the permittivity constant at constant stress.

The piezoelectric coefficient d_{31} is defined in the direction along the PVDF print traces, the d_{32} coefficient is defined perpendicular to the print traces and the d_{33} coefficient is defined in the direction of the film thickness (Fig 1). The 33 mode response is described as the out-of-plane mode, whereas the 31 and 32 modes are described as the in-plane modes. In the out-of-plane mode, the applied force is parallel to the generated electric field, whereas in the in-plane response, the force is applied perpendicular to the generated electric field. All three modes of operation are investigated in this work.

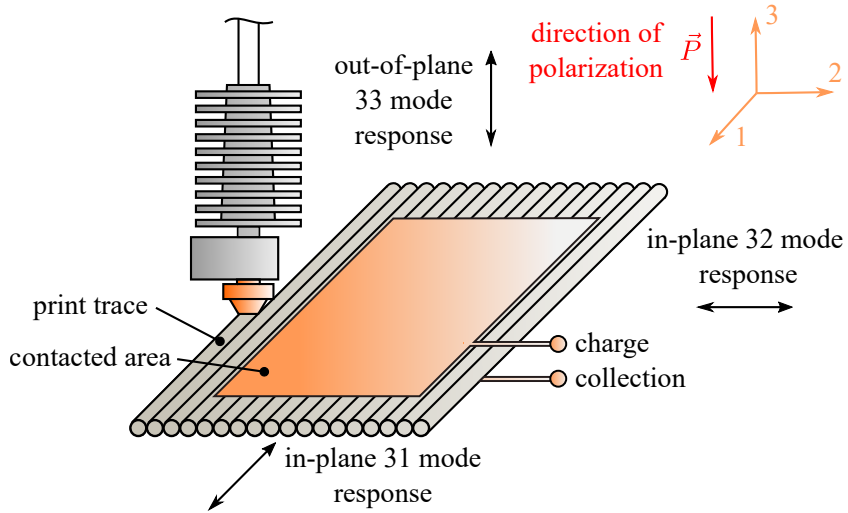


Figure 1: Coordinate system and mode response directions for a FFF piezoelectric PVDF film.

3. Dynamic Sensor Design

The dynamic sensor is designed to obtain a good measurable sensitivity at time-varying loads with respect to the manufacturing techniques. The 3D-printed dynamic sensor involves two steps: FFF and electrode poling.

The basic design of the single-process, 3D-printed dynamic sensor is shown in Fig. 2. Four different materials were used in the FFF: PVDF from Nile Polymers, Electrifi from Multi3D, HTPRO PLA from Plastika Trček, and TPU from Plastika Trček. The PVDF piezoelectric film is contacted with electrodes made from a conductive Electrifi filament. Each electrode contains short, wire-like traces that lead to the side of the sensor, which are later used for electrically contacting the copper wires. TPU is used as an electrode support to ensure that during the printing and poling processes, the semi-melted Electrifi stays in place. Mechanical compliance is another reason to use the TPU material. To ensure PVDF film bears the majority of the applied in-plane load and thus increasing sensor sensitivity, the rest of the materials in the region of the active PVDF film have to be as compliant as possible. High-temperature HTPRO PLA is used in the non-active parts of the sensor, where relative rigidity is needed and the induced stresses in the structure are high. It is used in anchors, designed to fix the sensor into the testing equipment, described later. HTPRO PLA also provides adequate bonding with the PVDF layers. Additionally, HTPRO PLA and TPU function as a support structure for the non-contacted area of the PVDF film.

In the next step, the sensor is poled using 3D-printed electrodes right after the fabrication, as seen in Fig 3. The sensors electrode wires are printed directly on the conductive copper tape, which is connected to the high-voltage

supply. With the proposed method, poling can be utilized directly on the 3D printer after FFF within a single process.

Fig. 2 contains the relevant dynamic sensor dimensions needed to calculate the piezoelectric coefficients of the PVDF film later on. According to the research in [25], the highest percentage of β phase was produced in 0.15-mm-thick FFF PVDF films. Due to printability issues, in this research the PVDF film had a thickness of 0.2 mm, as this provided the most consistent film with the fewest defects, while still containing a good amount of β phase according to the results in [25]. For details see the discussion. The thickness of the Electrifi electrodes were chosen to be 0.2 mm, in order to ensure continuous conductive traces, while minimizing the cross-sectional area of the non-piezoelectric layers to increase the sensor's sensitivity. The layer heights of the HTPRO PLA and TPU are governed by the thickness of the PVDF and Electrifi layers.

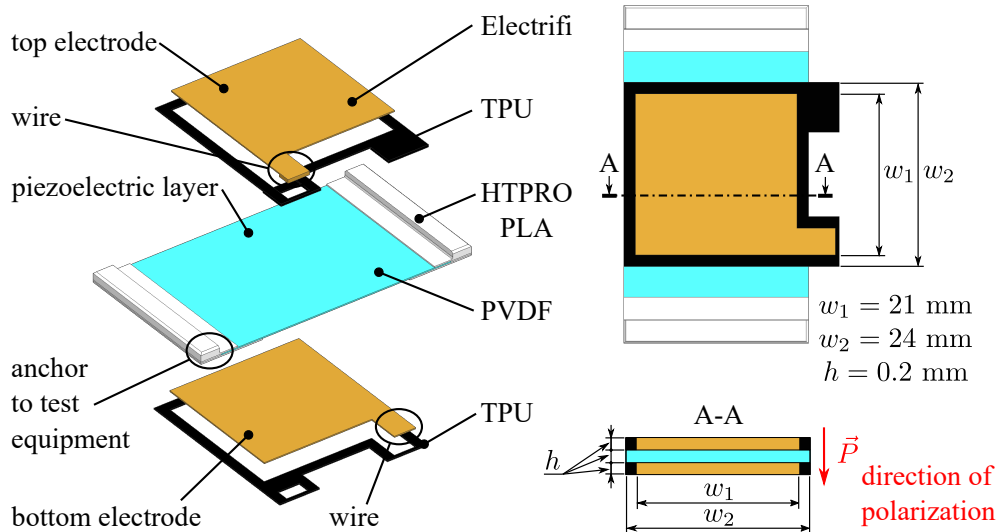


Figure 2: Single-process FFF dynamic sensor design with selected dimensions.

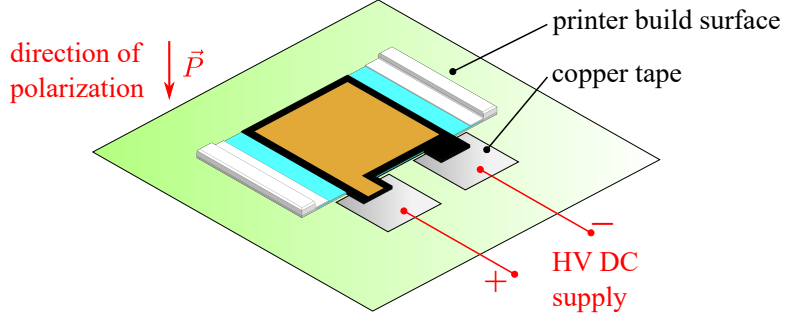


Figure 3: Sensor poling: Electrifi wire traces are deposited directly on the copper conductive tape connected to the HV power supply.

4. Experimental Methods

4.1. Sensor Fabrication

E3D Toolchanger was used to fabricate the dynamic sensor. It contains four different Matrix extruder tools from Trianglelab, which ensure each filament is extruded with its own nozzle to prevent mixing and contamination of the filaments. Each nozzle has a diameter of 0.4 mm and a layer height of 0.2 mm was used for all the layers and materials. Other printing parameters used to fabricate the dynamic sensor are listed in Tab. 1. Blue 3M tape with a thin layer of Elmer's purple glue stick was used for the adhesion of the sensor to the printer bed. Since Electrifi's conductive properties are prone to degradation if the material is kept at higher temperatures for long periods of time [27], the printer bed was kept at room temperature. The g-code file for the FFF was prepared using Prusa Slicer 2.3.0 with the profile configured for the E3D Toolchanger machine.

Table 1: Print parameters for sensor FFF fabrication.

Filament	Print Speed [mm/s]	Extrusion Rate [%]	Cooling Setting [%]	Extrusion Width [mm]	Heated Bed [°C]	Print Temperature [°C]
HTPRO PLA	50	94	100	0.45	25	210
PVDF	17	100	0	0.45	25	250
Electrifi	17	90	100	0.45	25	145
TPU	14	92	80	0.45	25	230

During initial trials of the sensor fabrication it was discovered that PVDF, compared to other materials, exhibits a relatively high coefficient of thermal expansion and is therefore prone to warping. This caused the sensor to detach from the print bed, and hence brims were used at the locations where the sensor detached from the bed. Additionally, it was found that in the direction of the trace deposition, the inner part of the PVDF film is smoother than the external part of the film. In other words, the PVDF traces form a rough film approximately 4 mm from the 180° change in the printing direction. Since a smooth PVDF film is desired for the piezoelectric sensing [14], two designs are proposed: the 31-mode and the 32-mode. The main difference between the sensor designs is the angle of the PVDF trace deposition with respect to the in-plane loading direction, as seen Fig. 4. Both designs ensure that only the smooth part of the PVDF film is electrically contacted with the Electrifi electrodes, thus ensuring the best possible contact surface. For the 32-mode design, the electrode wires are moved to the sides, to ensure the PVDF film is printed properly. Before the sensor fabrication, the copper tape guides,

visible in Fig. 4, are deposited on the printer build surface using HTPRO PLA. Two pieces of copper conductive tape from 3M are then placed within the guides, where Electrifi wire traces are deposited in the next step. An example of a FFF 3D-printing sequence is shown in Figure 5 for the 31-mode sensor design. After approximately 15 minutes, the sensor is ready to be poled via electrode poling.

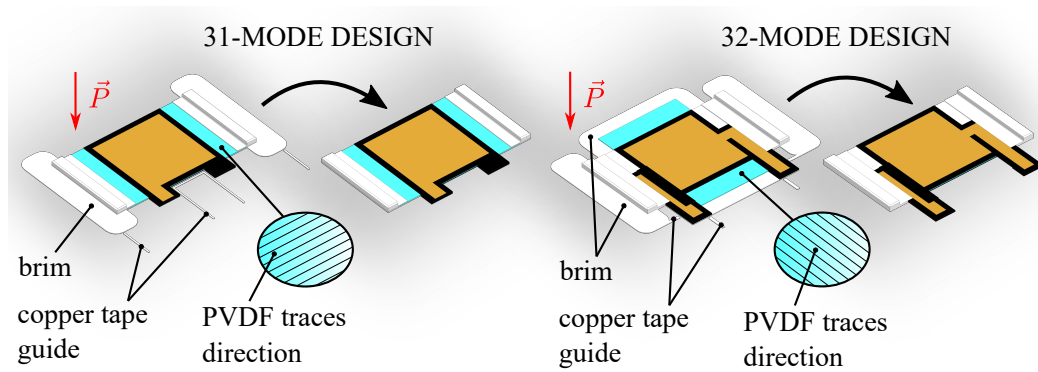


Figure 4: 31-mode and 32-mode dynamic sensor designs: As printed and without brims.

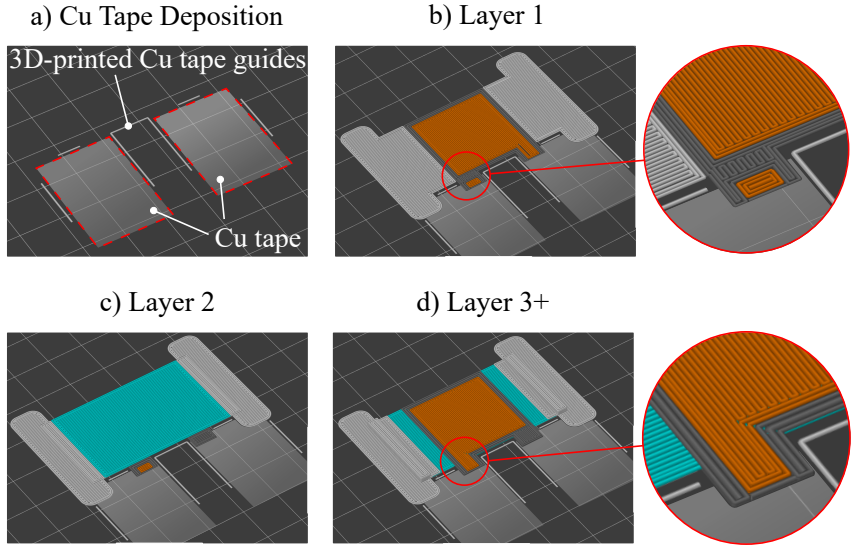


Figure 5: FFF 3D printing sequence of the 31-mode sensor design.

4.2. Electrode Poling

As the next step after the sensor's fabrication, electrode poling is utilized to polarize the sensor's PVDF film in the direction of its thickness. Various typical poling techniques for FFF-printed piezoelectric films are: electrode poling [18], corona poling [19], electric poling-assisted additive manufacturing (EPAM) [26] and the Integrated 3D printing and Corona (IPC) poling process [15]. Here, electrode poling is used, where the printed Electrifi traces act as electrodes. In contrast to corona poling, EPAM and IPC, electrode poling is not limited to poling in the z axis of the 3D-printer axes.

The poling process is carried out by supplying high-voltage direct current (HVDC) to the copper conductive-tape electrodes. The upper sensor electrode is electrically connected to the high-voltage supply and the bottom sen-

sor electrode (bed side) is grounded. A HVDC converter (Ultra 15AV12-P4, Advanced Energy) provides the voltage and current monitoring. The values were measured with a National Instruments (NI) 9215 data-acquisition card (DAQ). The high voltage was controlled with a NI 9263 analog output card.

Due to the short-circuit of the sensors during poling (see Sec. 6), the poling duration was chosen to be 14 minutes. The poling process is initially current and then voltage controlled and performed in four steps, as described in the following. In the first step, the bed is heated from room temperature to 90°C, close to the PVDF Curie temperature [16]. After 4 minutes, when a stationary temperature field across the sensor is reached, the second poling step is started, where the voltage is gradually increased to 3.3 kV, while the poling current is kept constant at 0.2 mA. In the third poling step, the voltage is kept constant at 3.3 kV until the combined duration of the second and third steps is equal to 10 minutes. The final poling voltage of 3.3 kV was chosen, since that is the highest value that the sensor could sustain without any arcing. The applied voltage is equivalent to an electric field of 16.5 MV/m.

After the sensor was successfully poled at the maximum possible electric field without any short circuiting, the sensor is removed from the printer's hot heated bed along with the spring-steel sheet and left to cool. After the sensor is cooled to room temperature, it is removed together with the 3M blue tape. Finally, the 3M blue tape is carefully removed from the sensor to ensure the bottom Electrifi electrode remains undamaged. Lastly, the brims are removed using an x-acto knife.

4.3. Electrical Contacts to the Measurement Setup

While the electrodes are 3D printed (Fig. 6), the electrical contacts are prepared by hand in a similar manner as reported in [28]. The sensor’s wire traces are, in the first step, coated with the conductive silver paint from Electrolube. In the second step, a thin enamelled copper wire is soldered to the conductive copper tape from 3M, which is then taped to the silver-paint-coated Electrifi traces. Optionally, the contact is additionally secured with another strip of copper tape, as shown in Fig. 6.

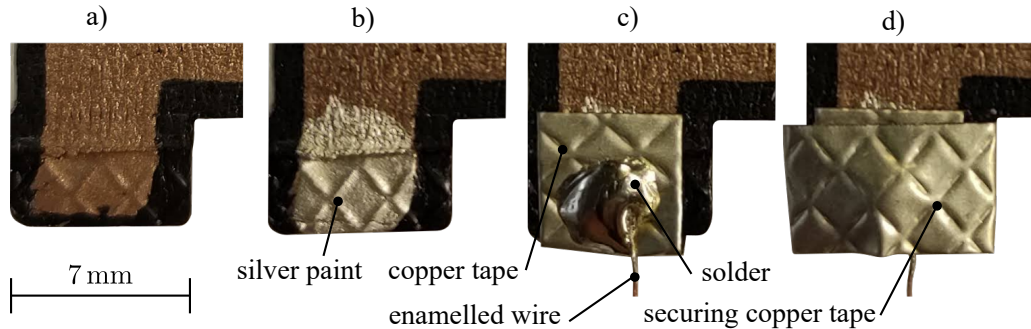


Figure 6: Electrical contacting: a) Printed sensor. b) Application of silver paint. c) Taping of copper conductive tape with copper wire. d) Application of additional copper tape.

4.4. Measuring the Sensor’s Sensitivity

Fig. 7 shows the experimental setup used to measure the sensor’s sensitivity. A SUPT Motion VCAR0022-0098-00A linear motor is used to apply the harmonic force to the sensor. The sensor fixation mechanism is fastened to the linear motor on the bottom and to a fixed support on the top. Two custom 3D-printed fixtures for the in-plane and out-of-plane sensitivity measurements visible in Fig. 7 were used. In both fixation mechanisms, the dynamic sensor is preloaded, to avoid buckling in the in-plane measurements

and to ensure a proper contact area in the out-of-plane measurements. The fixation for the in-plane sensing therefore anchors the sensor in place and provides a pre-tension of approximately 10 N, whereas the fixation for the out-of-plane sensing clamps the sensor in place and provides a compression force of approximately 10 N. In order to transfer the majority of the applied force from the linear motor to the sensor, the C-shaped springs are designed to be approximately 250 times more compliant than the 3D-printed sensor. To measure the force applied to the sensor, two PCB 208C01 force sensors (ICP type, range of ± 40 N) are placed on the sides of the fixtures (one sensor on each side, see Fig. 7). The 3D-printed sensor's electrodes are connected to the Brüel & Kjær Nexus 2692 charge amplifier to collect the generated charge on the sensor's PVDF film. In order to reduce the electromagnetic interference noise from the surroundings, the sensor is enclosed with a Faraday cage, see Fig. 7. The linear motor is driven in an open loop using a Pionner GM-A5702 audio amplifier connected to a NI 9263 analog output card.

The in-plane and out-of-plane sensitivity measurements of the specimens are taken approximately 24 hours after the poling process. The sinusoidal force with a frequency of 20 Hz at amplitudes ranging from 0.55 N to 2.55 N is applied to each sensor specimen. The measurement duration is 5 seconds. The measured charge $Q(t)$ and force $F(t)$ are converted from the time domain to the frequency domain using the Fourier transform. Assuming a linear system [29], the charge and force amplitudes at the excitation frequency ω_1 can be approximated with a linear regression:

$$|\hat{Q}(\omega_1)| = k \cdot |\hat{F}(\omega_1)| \quad (3)$$

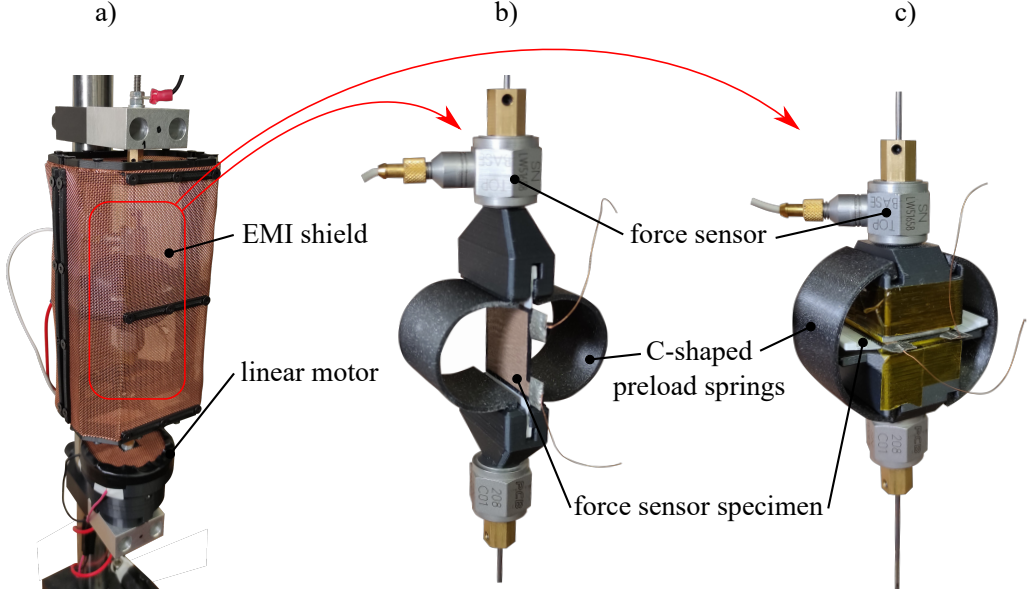


Figure 7: a) Electromagnetic interference shield and linear motor. b) In-plane sensitivity measurement. c) Out-of-plane sensitivity measurement.

where $\hat{Q}(\omega)$ and $\hat{F}(\omega)$ are the charge and force Fourier transforms, and the slope k is the sensitivity of the sensor. The phase shift between $Q(t)$ and $F(t)$ was found to be negligible.

5. Results

5.1. Sensor Fabrication

The two versions of the FFF 3D-printed dynamic sensors are visible in Fig. 8 and their fabrication process is shown layer by layer in Fig. 9. A total of twelve 31-mode and ten 32-mode dynamic sensors were manufactured. Due to the internal stresses developed in the 3D-printing process and the materials having different coefficients of thermal expansion, the fabricated

sensors are slightly curved after they are removed from the bed.

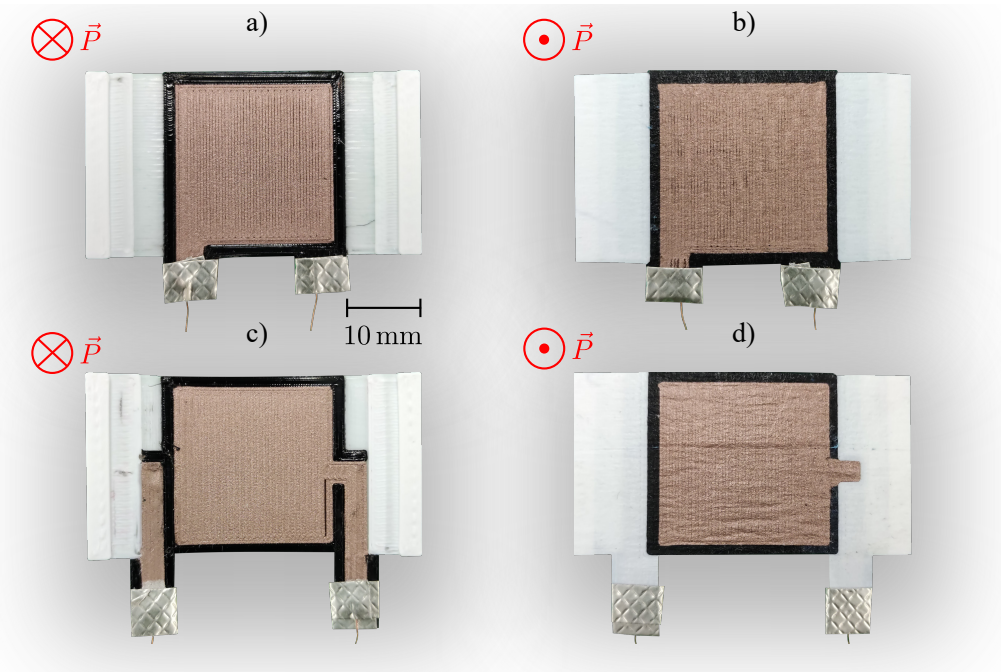


Figure 8: Dynamic sensors after FFF, electrode poling and electrical contacting with wires:
a) 31-mode design - top view, b) 31-mode design - bottom view, c) 32-mode design - top view, d) 32-mode design - bottom view.

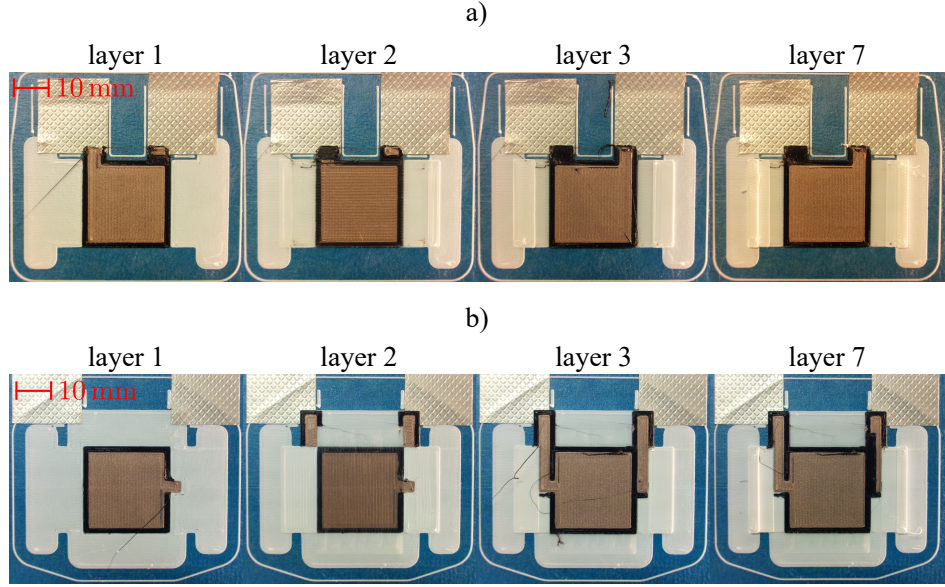


Figure 9: FFF shown layer by layer: a) 31-mode design, b) 32-mode design.

5.2. Electric Poling

An example of a successful poling process can be seen in Fig. 10. In the first step, the sensor achieves the desired stationary temperature field; in the second step the poling process is current controlled; and in the third step, where the final poling voltage value reaches 3.3 kV, the process is voltage controlled. The electric field applied to the specimens was 16.5 MV/m, which is on the lower side of conventional poling methods [14]. Consequently, the electric poling field is lower than the PVDF coercive field of approximately 41 MV/m, as reported in [30] at a poling temperature of 90°C. Increasing the electric field further resulted in arcing, due to the air gaps present in the PVDF films (see Sec. 6). During the poling process, the sensor was additionally heated up, due to the poling current and the Ohmic losses (the result of

the resistance of the electrodes), which increased the sensor's temperature. The temperature field was measured on the sensor's top electrode using an infrared (IR) camera. Fig. 10 shows the temperature averaged over the surface of the electrode during second and third steps of the poling process. A total of six 31-mode sensors and four 32-mode sensors were successfully poled.

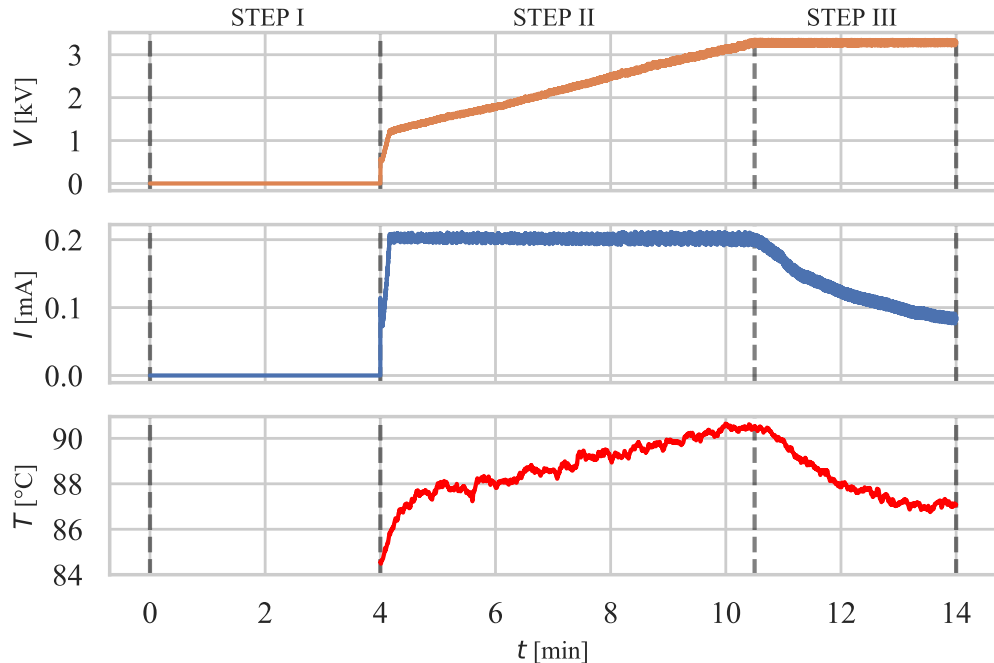


Figure 10: Electrode poling. Step I: the specimen is heated up. Step II: current-controlled poling. Step III: voltage-controlled poling.

5.3. Sensitivity Measurements

An example of the measured force F and charge Q time-domain signals used in sensitivity calculations is shown in Fig. 11. As a comparison, a time signal without electromagnetic interference shielding (EMI) is shown. The

amplitude spectra of the signals reveal that the electromagnetic interference noise is significantly reduced, see Fig. 12. It can be seen that the force induced on the sensor contains higher harmonics of the excitation frequency, which were found to result from the friction in the linear motor bearings.

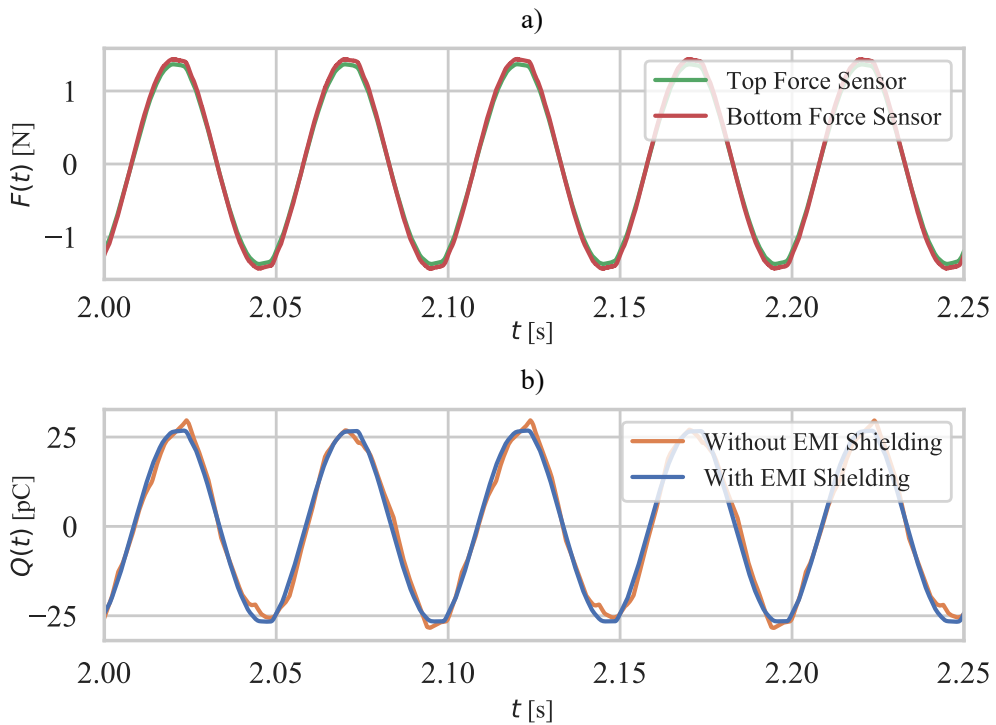


Figure 11: Measured sensor response: a) excitation force (PCB 208C01), b) charge generated by 31-mode design specimen.

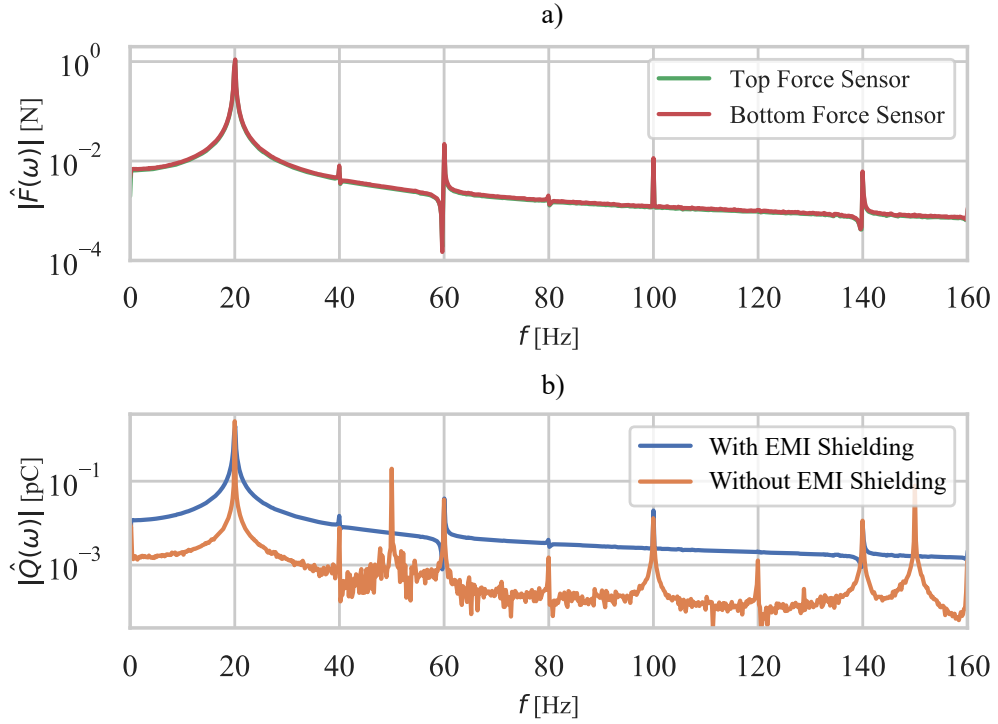


Figure 12: Amplitude spectra of the sensor response: a) excitation force (PCB 208C01), b) charge generated by 31-mode design specimen.

Relations between the force $|\hat{F}(\omega_1)|$ and the charge $|\hat{Q}(\omega_1)|$ amplitudes for the in-plane and out-of-plane measurements of all the specimens are shown in Fig. 13. Each specimen exhibits a clear linear relationship between the force applied to the sensor and the charge generated. However, due to the fabrication uncertainty, a slight variation in sensitivity between different sensor specimens is observed. The results are discussed in detail under Sec. 6. Tab. 2 shows the identified in-plane $k_{in-plane}$ and out-of-plane sensitivity $k_{out-of-plane}$ listed in Tab. 2, see Eq. (3). It is clear that the in-plane sensitivity is an order of magnitude higher than the out-of-plane sensitivity. A better in-plane sensitivity of the 31-mode is observed, when compared to the

32-mode design. For each sensor-sensitivity coefficient, an R-squared quality of fit was calculated. The minimum value obtained across all directions and specimens was $R^2 = 0.998$. The reader should also note that the sensitivity measurements are not statistically viable, as the number of measured specimens is not sufficient.

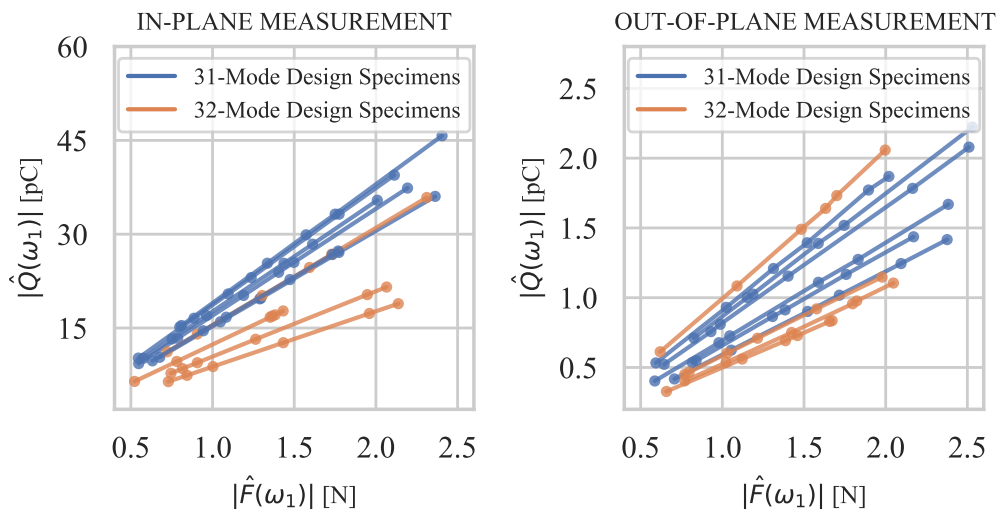


Figure 13: Relationship between the excitation force and the measured charge amplitudes for each dynamic sensor specimen.

Table 2: Sensor sensitivities averaged across six 31-mode and four 32-mode specimens.

Sensor Coefficient	Sensor Design			
	31-Mode		32-Mode	
	Mean	Max	Mean	Max
		Min		Min
$k_{in-plane}$ [pC/N]	17.2	19.0	11.8	15.5
		15.3		8.8
$k_{out-of-plane}$ [pC/N]	0.76	0.92	0.66	1.01
		0.59		0.50

5.4. PVDF Piezoelectric Coefficients Calculation

Calculations of piezoelectric coefficients based on measured sensor sensitivities is presented in Appendix A. Piezoelectric coefficients of the PVDF film are shown in Tab. 3. The estimated d_{33} coefficient value is the highest, followed by the d_{31} coefficient and, lastly, the d_{32} coefficient. Note that d_{33} was averaged from the 31-mode and 32-mode measurements.

Table 3: Piezoelectric coefficients of PVDF film averaged across all specimens.

Piezoelectric Coefficient	Value		
	Mean	Max	Min
d_{31} [pC/N]	0.44	0.49	
		0.39	
d_{32} [pC/N]	0.31	0.41	
		0.23	
d_{33} [pC/N]	0.72	1.01	
		0.50	

6. Discussion

In order for the sensor to function, it requires a perfect PVDF film layer, which is often difficult to achieve. A stock PVDF filament contains air bubbles, which cause porosity of the printed PVDF film, as shown in Fig. 14, since the extruder hotend melt zone is not fully filled with melted PVDF. It is also clear from Fig. 14 that most air gaps are visible to the naked eye. The porous film causes the Electrifi electrode layers to short circuit, in either the FFF or poling stage, resulting in a sensor malfunction. In order for the PVDF film traces to properly bond with each other, the sensor's first printed layer must have a uniform and smooth surface. Failure to do so results in air gaps along the PVDF traces, also visible in Fig. 14, which again leads to a short circuit between the electrodes. In order to decrease the porosity of the PVDF films as much as possible, the FFF process parameters of the PVDF were researched (not included in this manuscript). The optimal

process parameters obtained are shown in Tab. 1. Since the PVDF film's visible porosity is difficult to eliminate completely, a method for in-process part monitoring similar to the one described in [31] could be utilized to stop the fabrication of the sensor when a fault is detected. In the case where the bottom Electrifi electrode is printed with extrusion rates over 90%, material build-up between the traces is observed. Excess conductive material is then mixed with the deposited PVDF traces in the next layer, as the bottom Electrifi layer melts almost instantly when the PVDF trace is deposited above. It is theorized that excessive mixing of the PVDF traces with Electrifi leads to lower electric-field film-breakdown levels during the electric poling process.

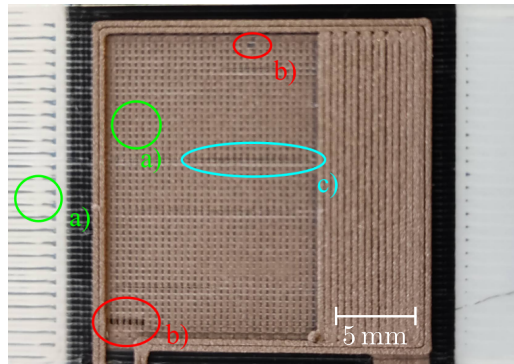


Figure 14: Possible sensor issues: a) imperfect first layer, b) air gaps due to air bubbles within PVDF filament, c) air gaps along the traces of PVDF film.

It is important to note that the Electrifi sensor electrodes become semi-melted during the poling process, which is the main contributing factor to the sensor failure modes that can be grouped into three different types. In the first failure-mode type, the Electrifi electrodes made electrical contact as soon as the specimen was heated up for the poling process. This failure mode is

only experienced in sensors containing larger air gaps in the PVDF films. The second group consists of the specimens that experience electrical breakdown in the smaller air gaps of the PVDF film during the second step of the poling process, when the voltage applied reaches a level of approximately 1000 V. The last failure-mode type occurs during the third step of the poling process, where the specimens are exposed to a final electric field for longer periods of time. It is suspected that the electrostatic force exerted on electrodes is (slowly) forcing the Electrifi to flow through the smaller air gaps, or is even opening new ones between the PVDF traces, causing the electrodes to short circuit. This failure mode was mostly avoided by decreasing the total poling time of the specimen from the initial 44 minutes to 14 minutes.

In the case of out-of-plane measurements, some specimens do not exhibit a perfect linear response. It is assumed that this is due to the sensor not having a perfectly smooth bottom and top electrode surface, where pressure was applied to the sensor. The contact area between each electrode and the surface applying the force is therefore changing, which introduces small levels of non-linearity.

Within each sensor-sensitivity direction, a fair amount of deviation is observed between the measured values. The FFF technique would be the first cause, since it is known to produce porous structures [32]. With different air gaps, the effective contact area between the PVDF film and the Electrifi electrodes changes, which affects the effective poling area of the film. The decreased poling area then results in decreased measured values of the in-plane and out-of-plane sensor sensitivities. The effective contact area increases with the extrusion rate used to deposit the Electrifi traces,

although that can also result in excessive built-up of the Electrifi material, which increases the risk of establishing electrical contact between the electrodes. On the other hand, the semi-melted state of the Electrifi along with the applied electrostatic force between electrodes during the electrode-poling process could also increase the effective contact area between the electrodes and the piezoelectric film.

The slightly lower in-plane sensitivity of the 32-mode dynamic sensor compared to the 31-mode dynamic sensor might also be a result of the differences in sensor design. The greatest difference between the designs is the relative angle between the traces of piezoelectric and conductive materials. In the 31-mode design, the traces are positioned with a relative angle of 90° , whereas in the 32-mode design, the relative angle is 0° . The relative angle could affect the airgaps present between the layers, hence impacting the contact area between the PVDF film and the Electrifi electrodes. This would result in a different poled effective area of the PVDF film, thus affecting the calculated value of the piezoelectric coefficients d_{31} and d_{32} .

The estimated piezoelectric coefficients of the single-process 3D-printed and poled PVDF film (Tab. 3) are an order of magnitude higher than those reported in [15] (IPC poling technique) and comparable to those reported in [14] (electrode poling in canola oil). Compared to commercially available PVDF films, manufactured with classic technology (piezoelectric coefficients up to $d_{33} = 30 \text{ pC/N}$ [32]), the d_{33} coefficient of PVDF layer of the FFF 3D-printed sensors is roughly 40 times lower.

The in-plane sensitivity of both dynamic sensor designs is sufficient to be used in a wide range of applications, such as structural health monitoring

and fatigue-crack detection [13]. If the sensor is calibrated beforehand and proper electromagnetic interference shielding is utilized, its sensitivity would also allow use in applications such as dynamic force measurements or even experimental modal analysis [33].

7. Conclusions

A method for a single-process FFF manufactured dynamic piezoelectric sensor is presented. It consists of two steps: FFF sensor fabrication and electrode poling under an electric field of 16.5 MV/m. During FFF, a piezoelectric PVDF film along with Electrifi electrode layers is manufactured. Using electrode poling, the sensor is poled in the same process on the printer bed.

During sensor-electrode poling, short circuiting of the electrodes is observed in some specimens, due to air gaps in the printed PVDF film in combination with the semi-melted Electrifi electrodes.

Two different sensor types named 31-mode design and 32-mode design were manufactured in order to measure the 31 and 32 piezoelectric mode responses. Based on simultaneous measurements of the excitation force and the generated charge, the in-plane and out-of-plane piezoelectric responses of two sensor designs were studied. For the 31-mode design and the 32-mode design, respectively, the in-plane sensitivities of approximately 17.2 pC/N and 11.8 pC/N and out-of-plane sensitivities of approximately 0.76 pC/N and 0.66 pC/N were measured. It was also shown that electromagnetic interference shielding reduces the noise of the measured charge signals.

Based on the in-plane and the out-of-plane sensor sensitivities, the averaged piezoelectric coefficients were identified: $d_{31} = 0.44 \text{ pC/N}$, $d_{32} =$

0.31 pC/N and $d_{33} = 0.72$ pC/N.

The proposed design principles for the FFF of piezoelectric sensors enable the design and manufacture of complex single-process sensor geometries in the future and offers the possibility to embed piezoelectric sensors in various FFF structures.

Acknowledgements

The authors acknowledge the partial financial support from the Slovenian Research Agency (research core funding No. P2-0263 and research project J2-1730).

Appendix A. PVDF Piezoelectric Coefficients Calculation

The sensor's sensitivity k can be used to obtain the d_{31} , d_{32} and d_{33} coefficients for the 31, 32 and 33 load mode responses, respectively. Assuming no external electric field ($E_k = 0$), the direct piezoelectric effect described by Eq. (2) is reduced for the 31, 32 and 33 mode responses to:

$$D_3(t) = d_{31} \sigma_1(t) \quad (\text{A.1})$$

$$D_3(t) = d_{32} \sigma_2(t) \quad (\text{A.2})$$

$$D_3(t) = d_{33} \sigma_3(t) \quad (\text{A.3})$$

From the electric displacement component $D_3(t)$, the generated charge $Q(t)$ can be obtained using:

$$Q(t) = \int_A D_3(t) \, dA = A D_3(t) = w_1^2 D_3(t) \quad (\text{A.4})$$

where A represents the area of the electrodes deposited on the piezoelectric film, w_1 represents the width of the squared electrode (see Fig. 2) and $D_3(t)$ is assumed constant across the area A . The stress induced in the 31, 32 and 33 mode responses can be calculated from the force time-domain signal as:

$$\sigma_1(t) = \frac{\eta F(t)}{w_1 h} \quad (\text{A.5})$$

$$\sigma_2(t) = \frac{\eta F(t)}{w_1 h} \quad (\text{A.6})$$

$$\sigma_3(t) = \frac{F(t)}{w_1^2} \quad (\text{A.7})$$

where h is the film thickness and η is the ratio between the forces induced in the cross-section of the active PVDF film and the cross-section of the whole sensor. η is derived by modelling different material segments (visible in the cross-section A-A in Fig. 2) as a series of springs connected in parallel:

$$\eta = \frac{w_1 E_{PVDF}}{w_2 E_{PVDF} + 2 w_1 E_{Electrifi} + 2 (w_2 - w_1) E_{TPU}} \quad (\text{A.8})$$

where E_{PVDF} , $E_{Electrifi}$ and E_{TPU} represent the Young's modulus of the PVDF, Electrifi and TPU, respectively. w_2 is the width of the whole sensor, see Fig. 2. Tab. A.4 contains the measured material properties used in the calculations. The Young's moduli were measured on beam-like cantilever specimens indirectly by measuring the density and the first natural frequency of each specimen. Layer height and raster angle of the specimens were the same as used in the 31-mode and 32-mode sensor designs, since they affect the effective Young's modulus [34].

Based on Eqs. (A.4), (A.5), (A.6) and (A.7), the piezoelectric coefficients of the PVDF can be identified from the measured force and charge as:

$$d_{31} = \frac{D_3(t)}{\sigma_1(t)} = \frac{\frac{Q(t)}{w_1^2}}{\frac{\eta F(t)}{w_1 h}} = \frac{h}{w_1 \eta} \frac{Q(t)}{F(t)} \quad (\text{A.9})$$

$$d_{32} = \frac{D_3(t)}{\sigma_2(t)} = \frac{\frac{Q(t)}{w_1^2}}{\frac{\eta F(t)}{w_1 h}} = \frac{h}{w_1 \eta} \frac{Q(t)}{F(t)} \quad (\text{A.10})$$

$$d_{33} = \frac{D_3(t)}{\sigma_3(t)} = \frac{\frac{Q(t)}{w_1^2}}{\frac{F(t)}{w_1^2}} = \frac{Q(t)}{F(t)} \quad (\text{A.11})$$

By transforming Eqs. (A.9), (A.10) and (A.11) into the frequency domain and using the sensor's in-plane and out-of-plane sensitivities, defined as $k_{in-plane} = |\hat{Q}(\omega_1)|/|\hat{F}(\omega_1)|$ and $k_{out-of-plane} = |\hat{Q}(\omega_1)|/|\hat{F}(\omega_1)|$, the piezoelectric coefficients are:

$$d_{31} = \frac{h}{w_1 \eta} \frac{|\hat{Q}(\omega_1)|}{|\hat{F}(\omega_1)|} = \frac{h}{w_1 \eta} k_{in-plane} \quad (\text{A.12})$$

$$d_{32} = \frac{h}{w_1 \eta} \frac{|\hat{Q}(\omega_1)|}{|\hat{F}(\omega_1)|} = \frac{h}{w_1 \eta} k_{in-plane} \quad (\text{A.13})$$

$$d_{33} = \frac{|\hat{Q}(\omega_1)|}{|\hat{F}(\omega_1)|} = k_{out-of-plane} \quad (\text{A.14})$$

Identifying piezoelectric the coefficients in the frequency domain reduces the effect of noise on the measurements.

Table A.4: Material properties of sensor materials used in the piezoelectric strain coefficient calculations.

Material	PVDF - 31-Mode Design	PVDF - 32-Mode Design	Electrifi	TPU
Young's Modulus [MPa]	1595	1564	1569	59

References

- [1] A. Kalkal, S. Kumar, P. Kumar, R. Pradhan, M. Willander, G. Packirisamy, S. Kumar, B. D. Malhotra, Recent advances in 3d printing technologies for wearable (bio)sensors, Additive Manufacturing (2021) 102088doi:<https://doi.org/10.1016/j.addma.2021.102088>. URL <https://www.sciencedirect.com/science/article/pii/S2214860421002530>
- [2] M. Juhasz, R. Tiedemann, G. Dumstorff, J. Walker, A. D. Plessis, B. Conner, W. Lang, E. MacDonald, Hybrid directed energy deposition for fabricating metal structures with embedded sensors, Additive Manufacturing 35 (2020) 101397. doi:<https://doi.org/10.1016/j.addma.2020.101397>. URL <https://www.sciencedirect.com/science/article/pii/S2214860420307697>
- [3] S. Bodkhe, G. Turcot, F. P. Gosselin, D. Therriault, One-step solvent evaporation-assisted 3d printing of piezoelectric pvdf nanocomposite structures, ACS Applied Materials & Interfaces 9 (24) (2017) 20833–

20842, pMID: 28553704. arXiv:<https://doi.org/10.1021/acسامی.7b04095>. doi:[10.1021/acسامی.7b04095](https://doi.org/10.1021/acسامی.7b04095).

URL <https://doi.org/10.1021/acسامی.7b04095>

- [4] D. Thuau, K. Kallitsis, F. D. Dos Santos, G. Hadzioannou, All inkjet-printed piezoelectric electronic devices: energy generators, sensors and actuators, *J. Mater. Chem. C* 5 (2017) 9963–9966. doi:[10.1039/C7TC02558K](http://dx.doi.org/10.1039/C7TC02558K).
URL <http://dx.doi.org/10.1039/C7TC02558K>
- [5] V. Zega, M. Invernizzi, R. Bernasconi, F. Cuneo, G. Langfelder, L. Muggaglini, M. Levi, A. Corigliano, The first 3d-printed and wet-metallized three-axis accelerometer with differential capacitive sensing, *IEEE Sensors Journal* 19 (20) (2019) 9131–9138. doi:[10.1109/JSEN.2019.2924473](https://doi.org/10.1109/JSEN.2019.2924473).
- [6] M. O. F. Emon, F. Alkadi, D. G. Philip, D.-H. Kim, K.-C. Lee, J.-W. Choi, Multi-material 3d printing of a soft pressure sensor, *Additive Manufacturing* 28 (2019) 629–638.
- [7] J. Xu, X. Zhang, Y. Liu, Y. Zhang, H.-Y. Nie, G. Zhang, W. Gao, Selective coaxial ink 3d printing for single-pass fabrication of smart elastomeric foam with embedded stretchable sensor, *Additive Manufacturing* 36 (2020) 101487. doi:<https://doi.org/10.1016/j.addma.2020.101487>.
URL <https://www.sciencedirect.com/science/article/pii/S2214860420308599>

- [8] G. L. Goh, H. Zhang, T. H. Chong, W. Y. Yeong, 3d printing of multilayered and multimaterial electronics: A review, *Advanced Electronic Materials* (2021) 2100445.
- [9] C. Lee, J. A. Tarbutton, Electric poling-assisted additive manufacturing process for PVDF polymer-based piezoelectric device applications, *Smart Materials and Structures* 23 (9) (2014) 095044. doi: 10.1088/0964-1726/23/9/095044.
URL <https://doi.org/10.1088/0964-1726/23/9/095044>
- [10] M. Marandi, J. Tarbutton, Additive manufacturing of single- and double-layer piezoelectric pvdf-trfe copolymer sensors, *Procedia Manufacturing* 34 (2019) 666–671, 47th SME North American Manufacturing Research Conference, NAMRC 47, Pennsylvania, USA. doi:<https://doi.org/10.1016/j.promfg.2019.06.194>.
URL <https://www.sciencedirect.com/science/article/pii/S2351978919309230>
- [11] C. J. Hohimer, G. Petrossian, A. Ameli, C. Mo, P. Pötschke, 3d printed conductive thermoplastic polyurethane/carbon nanotube composites for capacitive and piezoresistive sensing in soft pneumatic actuators, *Additive Manufacturing* 34 (2020) 101281. doi:<https://doi.org/10.1016/j.addma.2020.101281>.
URL <https://www.sciencedirect.com/science/article/pii/S2214860420306539>
- [12] M. Arh, J. Slavič, M. Boltežar, Design principles for a single-process 3d-printed accelerometer – theory and experiment, Me-

- chanical Systems and Signal Processing 152 (2021) 107475.
doi:<https://doi.org/10.1016/j.ymssp.2020.107475>.
- URL <https://www.sciencedirect.com/science/article/pii/S088832702030861X>
- [13] M. Palmieri, J. Slavič, F. Cianetti, Single-process 3d-printed structures with vibration durability self-awareness, Additive Manufacturing 47 (2021) 102303. doi:<https://doi.org/10.1016/j.addma.2021.102303>.
- URL <https://www.sciencedirect.com/science/article/pii/S2214860421004619>
- [14] D. A. Porter, T. V. Hoang, T. A. Berfield, Effects of in-situ poling and process parameters on fused filament fabrication printed pvdf sheet mechanical and electrical properties, Additive Manufacturing 13 (2017) 81–92. doi:<https://doi.org/10.1016/j.addma.2016.11.005>.
- URL <https://www.sciencedirect.com/science/article/pii/S2214860416303281>
- [15] H. Kim, F. Torres, Y. Wu, D. Villagran, Y. Lin, T.-L. Tseng, Integrated 3d printing and corona poling process of PVDF piezoelectric films for pressure sensor application, Smart Materials and Structures 26 (8) (2017) 085027. doi:[10.1088/1361-665x/aa738e](https://doi.org/10.1088/1361-665x/aa738e).
- URL <https://doi.org/10.1088/1361-665x/aa738e>
- [16] A. Jain, P. K. J., A. K. Sharma, A. Jain, R. P.N, Dielectric and piezoelectric properties of pvdf/pzt composites: A review, Polymer Engineering & Science 55 (7) (2015) 1589–1616. arXiv:

- <https://onlinelibrary.wiley.com/doi/pdf/10.1002/pen.24088>,
doi:<https://doi.org/10.1002/pen.24088>.
- URL <https://onlinelibrary.wiley.com/doi/abs/10.1002/pen.24088>
- [17] S. O. R. Moheimani, A. J. Fleming, Piezoelectric transducers for vibration control and damping, Springer, London, 2006.
- [18] The Effects of Additive Manufacturing and Electric Poling Techniques on PVdF Thin Films: Towards 3D Printed Functional Materials, Vol. ASME 2020 Conference on Smart Materials, Adaptive Structures and Intelligent Systems of Smart Materials, Adaptive Structures and Intelligent Systems, v001T04A010. arXiv:<https://asmedigitalcollection.asme.org/SMASIS/proceedings-pdf/SMASIS2020/84027/V001T04A010/6588106/v001t04a010-smasis2020-2245.pdf>,
doi:10.1115/SMASIS2020-2245.
- URL <https://doi.org/10.1115/SMASIS2020-2245>
- [19] S. K. Mahadeva, J. Berring, K. Walus, B. Stoeber, Effect of poling time and grid voltage on phase transition and piezoelectricity of poly(vinylidene fluoride) thin films using corona poling, Journal of Physics D: Applied Physics 46 (28) (2013) 285305. doi:10.1088/0022-3727/46/28/285305.
- URL <https://doi.org/10.1088/0022-3727/46/28/285305>
- [20] M. Lee, C.-Y. Chen, S. Wang, S. N. Cha, Y. J. Park, J. M. Kim, L.-J.

- Chou, Z. L. Wang, A hybrid piezoelectric structure for wearable nano-generators, *Advanced Materials* 24 (13) (2012) 1759–1764.
- [21] S. Y. Chung, S. Kim, J.-H. Lee, K. Kim, S.-W. Kim, C.-Y. Kang, S.-J. Yoon, Y. S. Kim, All-solution-processed flexible thin film piezoelectric nanogenerator, *Advanced Materials* 24 (45) (2012) 6022–6027.
- [22] G. L. Goh, M. F. Tay, J. M. Lee, J. S. Ho, L. N. Sim, W. Y. Yeong, T. H. Chong, Potential of printed electrodes for electrochemical impedance spectroscopy (eis): Toward membrane fouling detection, *Advanced Electronic Materials* (2021) 2100043.
- [23] F. Li, W. Liu, C. Stefanini, X. Fu, P. Dario, A novel bioinspired pvdf micro/nano hair receptor for a robot sensing system, *Sensors (Basel, Switzerland)* 10 (2010) 994–1011. doi:10.3390/s100100994.
- [24] High resolution aerosol jet printing of conductive ink for stretchable electronics, Vol. International Conference on Progress in Additive Manufacturing (Pro-AM 2018). doi:10.25341/D4FS3W.
URL <https://hdl.handle.net/10356/88279>
- [25] N. Momenzadeh, Influences of material extrusion additive manufacturing (meam) parameters and additives on polyvinylidene fluoride (pvdf) properties., Ph.D. thesis, University of Louisville (2020).
- [26] C. Lee, J. Tarbutton, Polyvinylidene fluoride (pvdf) direct printing for sensors and actuators, *The International Journal of Advanced Manufacturing Technology* 104 (10 2019). doi:10.1007/s00170-019-04275-z.

- [27] T. Barši Palmić, J. Slavič, M. Boltežar, Process parameters for fff 3d-printed conductors for applications in sensors, Sensors 20 (16) (2020). doi:10.3390/s20164542.
URL <https://www.mdpi.com/1424-8220/20/16/4542>
- [28] M. Arh, J. Slavič, M. Boltežar, Experimental identification of the dynamic piezoresistivity of fused-filament-fabricated structures, Additive Manufacturing 36 (2020) 101493. doi:<https://doi.org/10.1016/j.addma.2020.101493>.
URL <https://www.sciencedirect.com/science/article/pii/S2214860420308654>
- [29] S. S. Rao, Mechanical Vibrations, 5th Edition, Prentice Hall, 2010.
- [30] R. Olsen, J. Hicks, M. Broadhurst, G. Davis, Temperature-dependent ferroelectric hysteresis study in polyvinylidene fluoride, Applied physics letters 43 (1) (1983) 127–129.
- [31] M. Moretti, A. Rossi, N. Senin, In-process monitoring of part geometry in fused filament fabrication using computer vision and digital twins, Additive Manufacturing 37 (2021) 101609. doi:<https://doi.org/10.1016/j.addma.2020.101609>.
URL <https://www.sciencedirect.com/science/article/pii/S2214860420309817>
- [32] I. Buj-Corral, A. Bagheri, M. Sivatte-Adroer, Effect of printing parameters on dimensional error, surface roughness and porosity of fff printed parts with grid structure, Polymers 13 (8) (2021). doi:10.

3390/polym13081213.

URL <https://www.mdpi.com/2073-4360/13/8/1213>

[33] J. M. M. Silva, N. M. M. Maia, Modal Analysis and Testing, 1st Edition, Springer Netherlands, 1999.

[34] G. D. Goh, Y. L. Yap, H. K. J. Tan, S. L. Sing, G. L. Goh, W. Y. Yeong, Process–structure–properties in polymer additive manufacturing via material extrusion: A review, Critical Reviews in Solid State and Materials Sciences 45 (2) (2020) 113–133. arXiv:<https://doi.org/10.1080/10408436.2018.1549977>.

URL <https://doi.org/10.1080/10408436.2018.1549977>